Indonesian Physical Review
Volume 07 Issue 03, September 2024
P-ISSN: 2615-1278, E-ISSN: 2614-7904

A GUI-Based Data Acquisition System for EIT Using Two Current Injection Methods

Ahmad Zarkasi[1*], Muhammad Fauzan Hananda Putra[1], Adrianus Inu Natalisanto[1], Kholis Nurhanafi[1], Muhammad Hidayatullah[2], Amirin Kusmiran[3], Amalia C. Nuraidha[4]

[1] *Department of Physics, Faculty of Mathematics and Natural Sciences, Universitas Mulawarman, Indonesia*
[2] *Department of Electrical Engineering, Faculty of Engineering, Universitas Teknologi Sumbawa, Indonesia*
[3] *Department of Physics, Faculty of Science and Technology, Universitas Islam Negeri Alauddin Makassar, Indonesia*
[4] *Department of Biomedical Engineering, Faculty of Science and Technology, Universitas PGRI Yogyakarta, Indonesia*

Corresponding Authors E-mail: ahmad.zarkasi@fmipa.unmul.ac.id

Article Info

Article info:

Received: 26-06-2024
Revised: 18-07-2024
Accepted: 24-07-2024

Keywords:

EIT; GUI; Boundary Potential; Current Injection

How To Cite:

A. Zarkasi, M. F. H. Putra, A. I. Natalisanto, K. Nurhanafi, M. Hidayatullah, A. Kusmiran, A. C. Nuraidha, "A GUI-Based Data Acquisition System for EIT Using Two Current Injection Method," Indonesian Physical Review, vol. 7, no. 3, p 379-397, 2024.

DOI:

https://doi.org/10.29303/ipr.v7i3.356

Abstract

The current injection method played an essential role in the data quality of impedance measurement using the electrical impedance tomography (EIT) technique. Previous studies have largely utilized only a single current injection method with limited interface access, which restricts the effectiveness of EIT systems. In this paper, a graphical user interface (GUI)-based data acquisition system was designed to improve user interaction and optimize the control system. The system was equipped with multiple current injection methods, allowing researchers to choose which method to use in the measurement process. The designed hardware comprises a V-to-I converter circuit, multiplexer, electrodes, peak detector, and filter circuit. Testing results indicate that the V to I converter circuit has an average peak difference between voltage and current of 4.86% and an average error of 0.69% in the peak detector circuit. The multiplexer circuit switches quickly and consistently, while the filter circuit remains stable at the 50 kHz frequency used in this study. These results demonstrate that the designed circuits perform adequately and effectively, ensuring reliable and accurate measurements. Additionally, the data acquisition software, presented as a GUI, effectively facilitates the selection of current injection methods and the display of boundary data simulation (BDS) on the object. This is demonstrated by the spatial inhomogeneity patterns visible through BDS in both the adjacent and opposite methods.

Introduction

Fundamentally, imaging techniques involve visual reconstruction based on specific treatments and the responses that occur in an object. Imaging is mostly applied in the medical field, which

analyzes the body's internal organs. Some of the imaging techniques in the medical field are X-ray, magnetic resonance imaging (MRI), and computerized tomography (CT-scan) [1].

Electrical impedance tomography (EIT) was developed as an imaging technique to visualize an object's internal conductivity distribution. The data acquisition process involves injecting an electric current through the object and measuring the potential or voltage around the object's surface [2], [3], [4], [5]. EIT is expected to be a significant competitor in imaging methods, especially medical imaging. Up until recently, EITs have been used for several applications, such as internal organ monitoring [6], [7], [8], [9], [10], [11], quality control and damage detection [12], [13], plant phenotyping [14], body gesture recognition [15], and portable health monitor [16].

EIT has some advantages, such as low cost, non-ionizing, and non-invasive [17], [18], [19], [20]. On the other hand, in terms of image quality and resolution, EIT needs better image quality due to its spatial limitations in the sensing process and sensitivity to small changes [21], [22], [23]. Moreover, EIT needs a challenging reconstruction algorithm as it is an ill-posed and non-linear inverse problem [3], [21], [24]. However, researchers made developments to overcome those drawbacks, mainly in the reconstruction process [11], [17], [25].

Several studies have attempted to improve sensitivity and reduce ill-posed conditions by increasing the number of electrodes. The number of electrodes has been increased to 32 or even more, which has been shown to improve the quality of the data generated [26], [27], [28]. A more significant number of electrodes results in better image resolution [21]. However, the use of too many electrodes is limited by the spatial conditions of the object [3]. Therefore, another widely considered solution was using a variation of the current injection method [29], [30], [31]. This solution was widely chosen. In addition to increasing the sensitivity of the measurement results, it was also a simpler and more economical option because it did not require additional costs, such as increasing the number of electrodes.

The EIT data acquisition system is divided into hardware and software. The hardware system consists of a current source, a multiplexing system, a set of electrodes, a signal conditioning, and the data reading instrument [22], [32], [33]. A microcontroller controls the system for automated processes, mainly in the multiplexing process and data [12], [19], [34]. The software consists of a data acquisition interface and an image reconstruction algorithm. The final data generated from the hardware is the boundary potential of the object acquired through the electrodes. This potential data is then processed to be displayed visually as an image or BDS. The manual data acquisition system certainly reduces measurement accuracy. It slows the EIT data acquisition process, while objects often sampled in conductivity measurements using EIT experience impedance changes quickly [35], [36]. Hence, an intuitive and effective interface is important in EIT data acquisition.

Most EIT data acquisition processes mainly use only a single current injection method [37], [38], [39]. Yet, as previously described, the current injection method greatly affected the measurement data quality [40]. In this paper, a graphical user interface (GUI)-based system with two current injection methods was designed. The use of GUI provided flexibility for users to explore the research further. This system allows users to freely obtain the current and EIT data using the best current injection method without different instrumentation adjustments.

Current Injection on EIT

Several studies have proposed approaches to improve measurement sensitivity, including increasing the number of electrodes [41], current injection method [42], and current amplitude [40], [42]. Theoretically, increasing the number of electrodes is an effective solution because more surface potentials are generated to be reconstructed. However, this would result in greater complexity in the data acquisition system and prolong the time required for data acquisition and image reconstruction. Thus, adjusting the injection method and current value is the most efficient choice. This strategy can be optimized without requiring much additional cost.

The frequency range commonly applied to the EIT method is quite wide at 1-100 kHz [5], [40], [43], [44], [45]. The dielectric component tends to be neglected in such a wide frequency range. This limits the impedance value to the conductivity value involving the resistance component. This is acceptable because the current is in a fixed state. If Ω is the domain of the conductivity distribution mapping, then based on Maxwell's equations, the potential distribution on the object satisfies Laplace's equation with boundary [46].

$$\begin{cases} \vec{\nabla} \cdot \left(\sigma(\vec{r}) \vec{\nabla} \vec{\phi}(\vec{r}) \right) = 0, (\vec{r}) \in \Omega \\ \sigma(\vec{r}) \vec{\nabla} \vec{\phi}(\vec{r}) \cdot \vec{n} = \vec{J}, (\vec{r}) \, \partial \in \Omega \end{cases} \tag{1}$$

In equation (1), σ is the internal conductivity; $\vec{\phi}(\vec{r})$ represents the potential at $\vec{r}$; $\vec{J}$ represents the injection current density and $\vec{n}$ is the normal direction. Specifically, equation (1) states that the divergence of the product between the internal conductivity and the potential gradient is zero inside the domain of the conductivity distribution mapping (Ω), meaning there is no source inside the object that generates an electric field inside. Explicitly, Equation (1) also explains that the potential gradient at the boundary of the object domain is parallel to the injection current. This means that the electric potential at the object's surface is directly affected by the current injected into the object. It describes the direct interaction between the injection current and the object's response to its conductivity distribution. Apart from the theoretical aspects, the empirical research results also corroborate the fact that the value of injection current also greatly affects the measurement sensitivity as well as the condition of the measuring object, as performed by [40], [42], [47].

Experimental Method

Hardware Development

The instrumentation of the data acquisition system consists of a signal generator, a V to I converter, a multiplexer, a circular container, a high pass filter circuit, a peak detector circuit, and a microcontroller (Figure 1).

A signal generator generates sinusoidal signals as an input to the system. We used a signal generator from the Feeltech brand, model FY6600. This signal generator uses DDS and can generate signals up to 60 MHz.

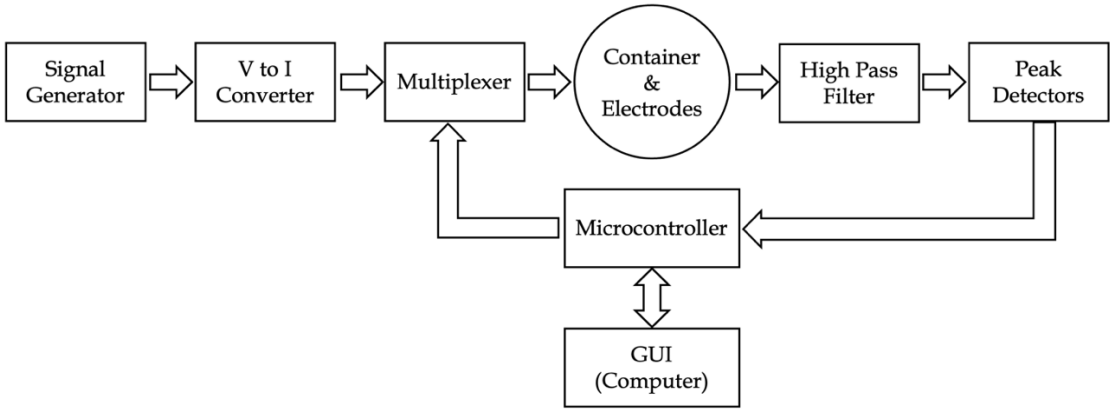

Figure 1. Block diagram design of EIT data acquisition system

Therefore, in terms of specifications, the signal generator is adequate for this research's use as a pulse source. The voltage generated from the signal generator must be converted to current before applying since the injection system is amperometric. In this study, we designed the V to I converter circuit ourselves. V to I converter circuit testing was performed by providing a load resistance of 1 kΩ. The current and voltage on a pure resistive material in the form of a resistor certainly have the same phase. With an input voltage of 1 V and a resistance of 1 kΩ, an output current of 1 mA is obtained. It can be seen from Figure 2 that the phase of the output voltage representing the current has the same phase, which means that the designed V to I converter circuit is feasible to apply. Although, based on our calculations, there is an average difference of 4.86% between the input and output voltage values, the overall difference is relatively small.

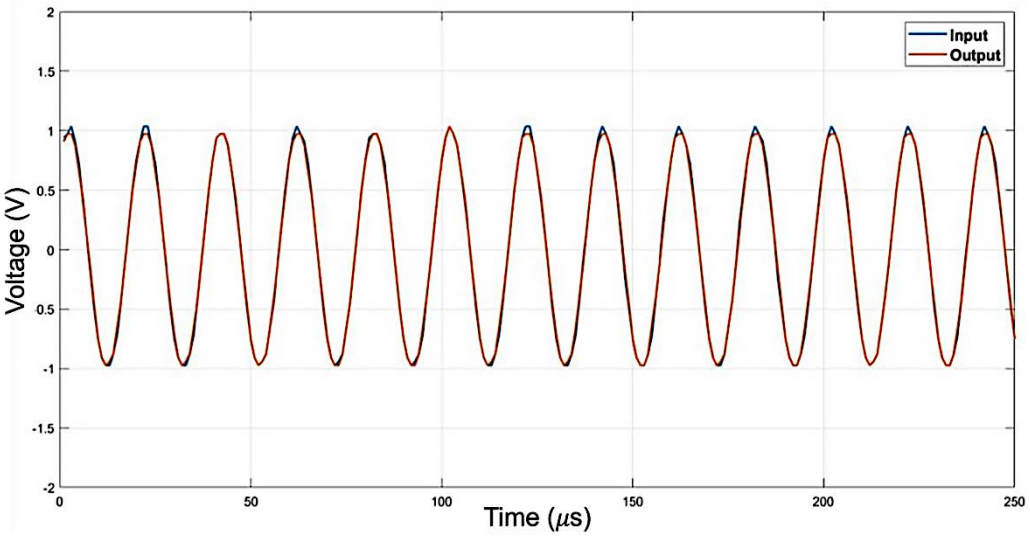

Figure 2. Test results of V to I converter circuit

The output current from the V to I converter circuit is then injected into the object/material through 8 electrodes mounted on a circular container made of a 2-inch diameter PVC pipe. The current injection is regulated through two multiplexers with a 74HC4051 chip. This chip was chosen because of its excellent switching speed and consistency. Figure 3 is the result of

testing the multiplexer circuit. Figure 3(a) is the result of testing on the current injection electrode, and Figure 3(b) is the result of testing on other electrodes.

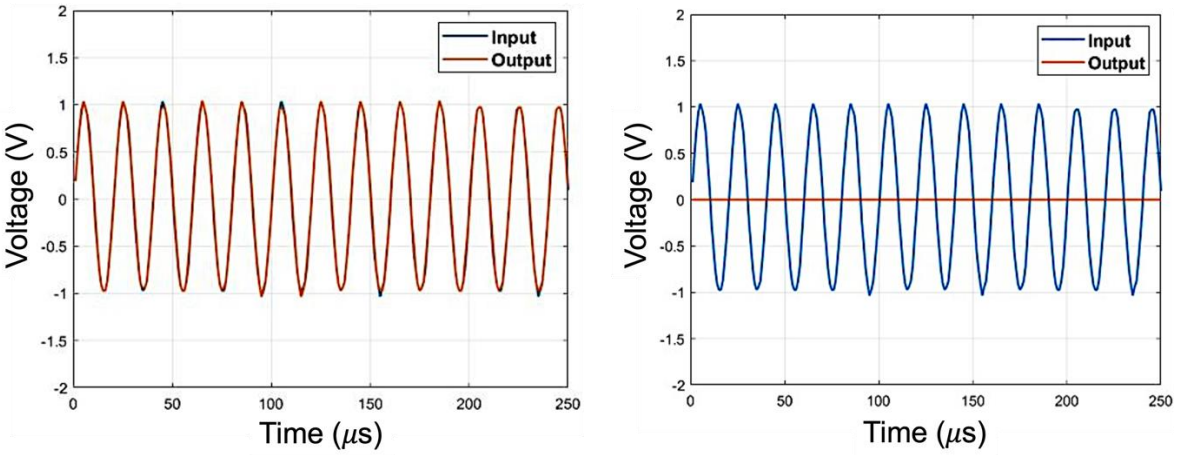

Figure 3. Multiplexer test results on (a) injection electrode and (b) other electrodes

Before being transmitted to the computer, the object's output voltage must be processed first. This requires a high pass filter (HPF) and peak detector circuits. HPF plays a role in preventing low frequency and DC signals that can be read in the measurement process and can also lead to signals that do not fluctuate at zero. Based on the test results (Figure 4), it can be seen that the output voltage read is stable in the frequency range of 2 kHz to 62.5 kHz with a voltage value of about 2 Vpp (peak-to-peak) and the output voltage at frequencies below 2 kHz is attenuated. This HPF circuit is suitable since the frequency used is only a single frequency value of 50 kHz.

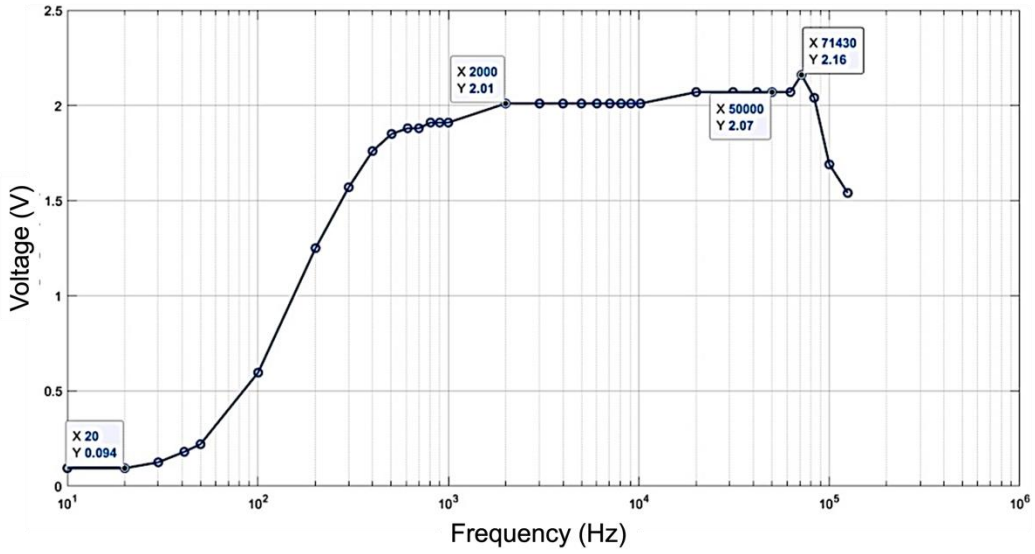

Figure 4. Frequency response test results on HPF

The object's signal is an alternating voltage, while the microcontroller can only read positive voltage values. Therefore, adding hardware as a peak detector circuit is very important. Figure 5 shows the test results of the peak detector circuit. It can be seen that the designed circuit can

read the peak quite well. Based on our calculations, there is a relatively small error of 0.69% on average.

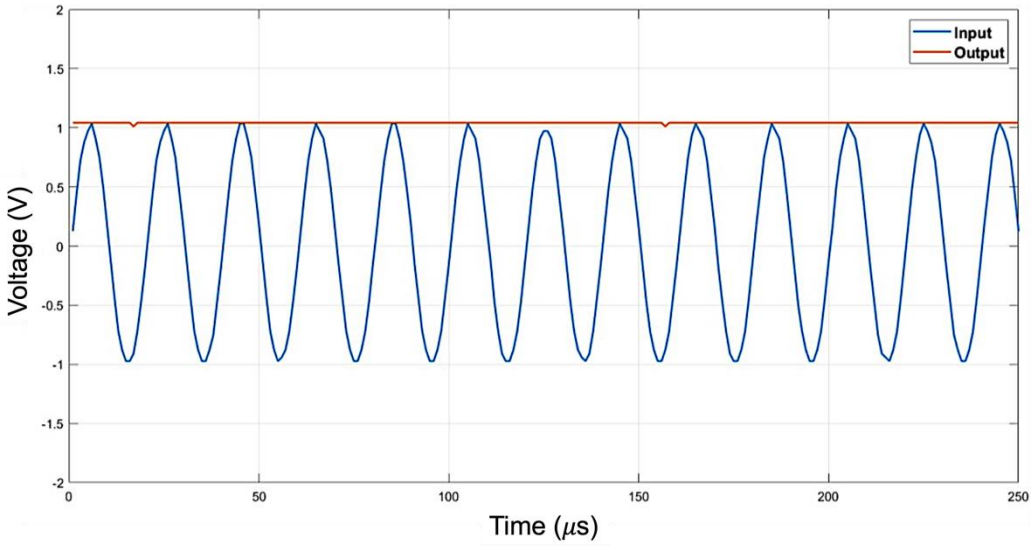

Figure 5. Testing results of peak detector circuit

After ensuring that all hardware components work properly, the entire circuit/elements are assembled. Figure 6 shows a photo of all the hardware used in this research (excluding the signal generator and power supply). Essentially, the hardware in this EIT system ensures that the signals read and processed by the software are accurate and not noise or aliasing signals. The Arduino Mega 2560 microcontroller manages the process control of multiplexing and data transmission. This microcontroller board was chosen because it has an adequate number of analog input pins, a large flash memory of up to 256 KB, and a high transmission speed.

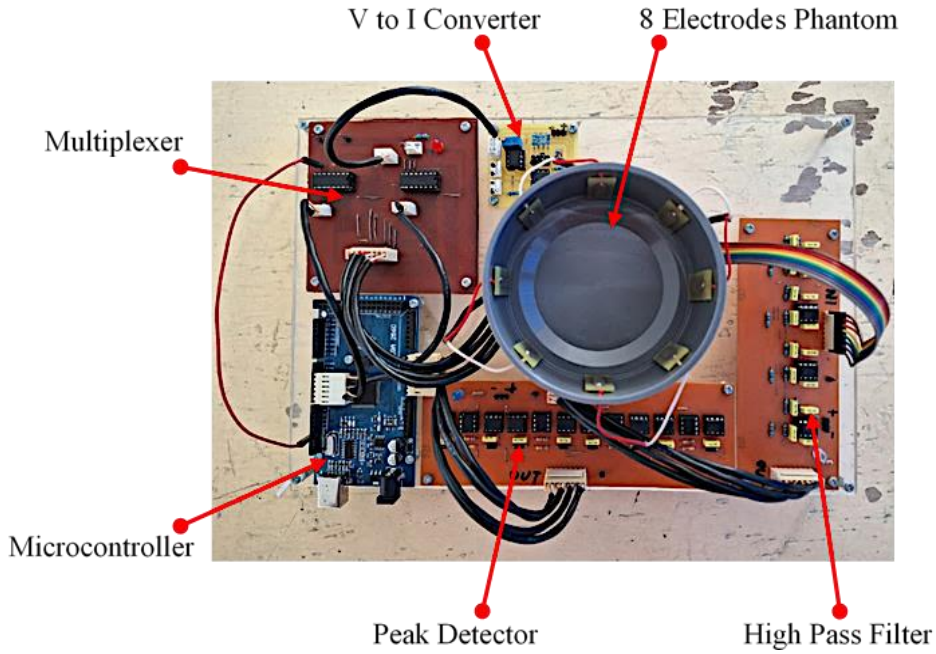

Figure 6. Hardware of EIT data acquisition system

Software Development

A graphical user interface (GUI) is used as an interaction media between the system and the user. In this case, the interaction is used to choose the current injection method and start the data acquisition process. The GUI was designed using MATLAB software, which includes a package to connect the microcontroller in the instrumentation system with MATLAB (Figure 7). The current injection methods provided in GUI are the adjacent and opposite methods. Acquired boundary potential data will be displayed as a table and visualized as a graph. Exporting the acquired data as a spreadsheet file for documentation is also possible.

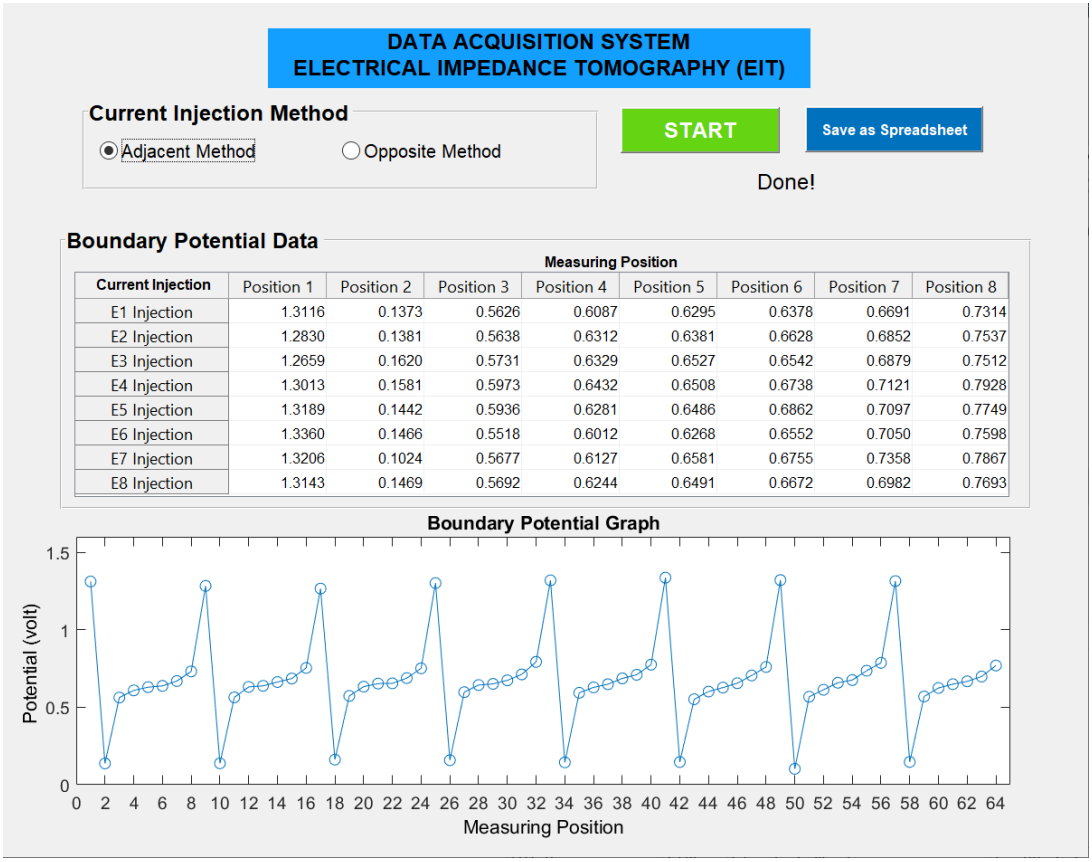

Figure 7. GUI design

Data Acquisition

For the data acquisition process, adjacent (Figure 8(a)) and opposite (Figure 8(b)) current injection methods compare the boundary potential data acquired by respective methods. The boundary potential value is measured from every electrode, including the current injection electrode, with ground as the reference voltage [5], [48], [49].

Current injection is executed through every adjacent or opposite pair of electrodes, and boundary potentials are measured from each electrode according to the current injection position and direction. The switching process is handled automatically by the multiplexer, which is programmed and controlled from the GUI.

In this experiment, an alternating current of 1 mA at 50 kHz is used, a common choice among EIT researchers [16], [27], [41], [50]. Mineral water was used as the reference liquid and placed

in a circular container. Measurements were taken under several conditions. The first condition is when no isolator/conductor object is in the container (Figure 9(a)). The data obtained under this condition is treated as a reference for comparison. The second condition is when the isolator is placed near one of the electrodes, specifically at electrode 3 (Figure 9(b)). The third condition is when the conductor is placed near one of the electrodes, specifically at electrode 7 (Figure 9(c)). The fourth condition is when the isolator and conductor are placed inside the container according to their positions in the previous condition (Figure 9(d)). It should be noted that the inhomogeneous object should be positioned near the inner curved surface, and the mineral water used for each condition should be of the same type and source. The obtained boundary potential data were plotted with the reference and inhomogeneous data stacked in the same graph. The data is expected to show the inhomogeneity pattern according to the position of the inhomogeneous isolator/conductor inside the container.

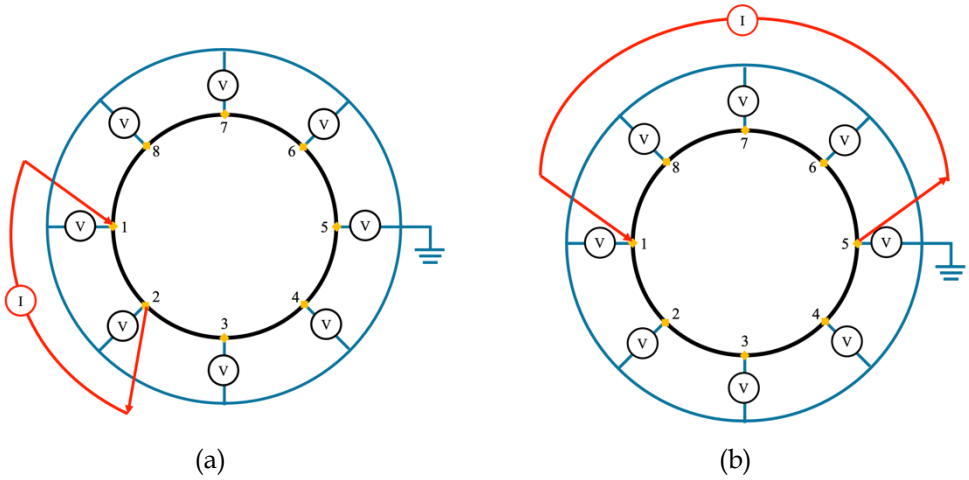

Figure 8. Current injection illustration of (a) adjacent method and (b) opposite method

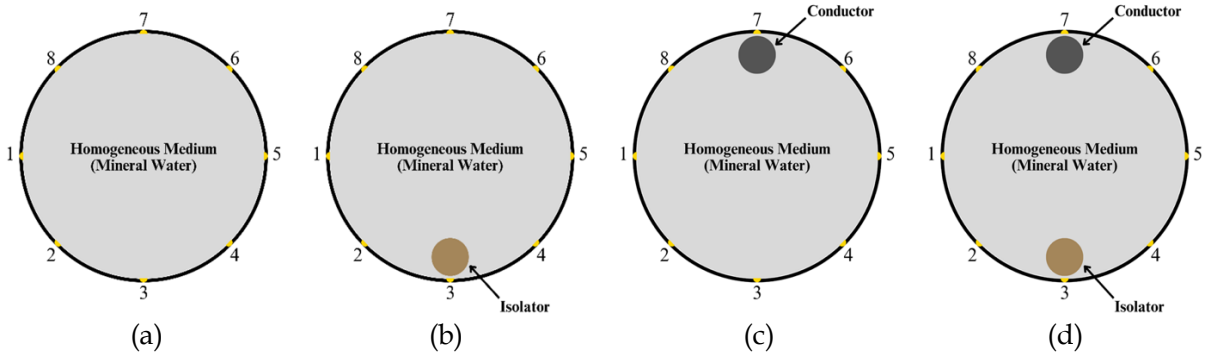

Figure 9. Measurement configuration with conditions (a) no isolator or conductor, (b) isolator placed near electrode 3, (c) conductor placed near electrode 7, and (d) isolator and conductor placed together.

Result and Discussion

The boundary potential data is acquired using the designed GUI system with 64 data points for each current injection method in each condition. Figures 10(a) and 10(b) show the boundary potential value measured in the first condition using adjacent and opposite methods, which becomes the reference data. The pattern that emerged every 8 measurement positions represents the boundary potential value for each iteration of the current injection

method. It can be seen that the value varies between the maximum and the minimum potential value. Based on the physics principle, an electric current flows from a higher electric potential point to a lower one. The graph shows that for every injection point and ground point electrode, its potential value reaches the maximum and the minimum. In contrast, the other electrodes have different potential values according to their position relative to the injection and ground point electrodes. However, some potential value differences in several measurement positions might be caused by a slight error in the electrode's symmetrical position or the condition of the electrode itself. Based on our calculations, we obtained a standard deviation of 0.0175 for the adjacent method, while for the opposite process, it was 0.0200. These standard deviation values are relatively small, so the difference in potential values at each electrode position can be neglected.

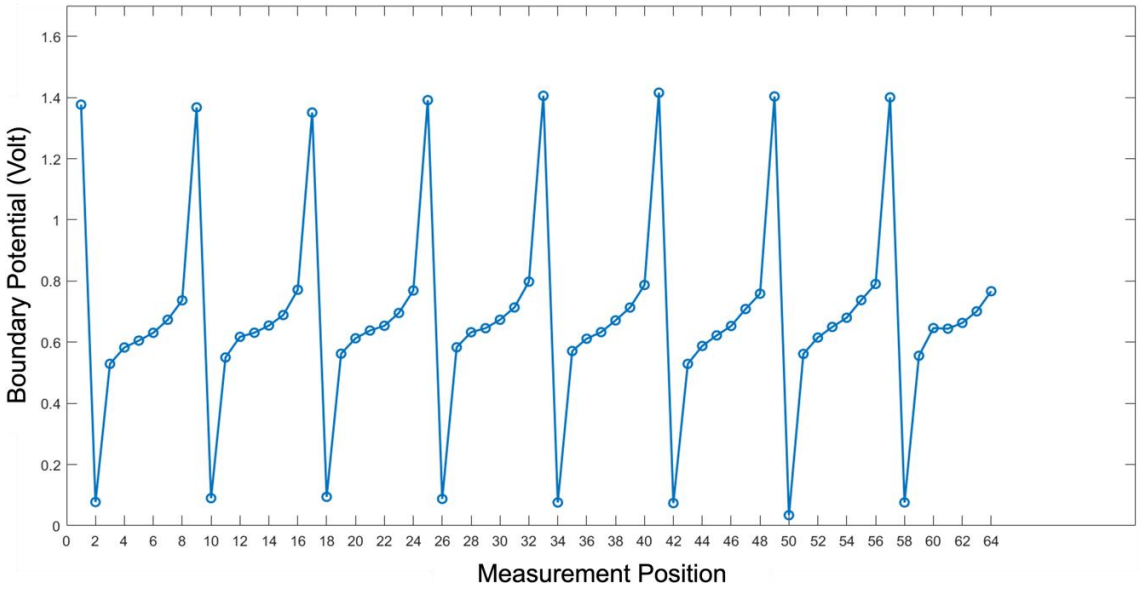

(a)

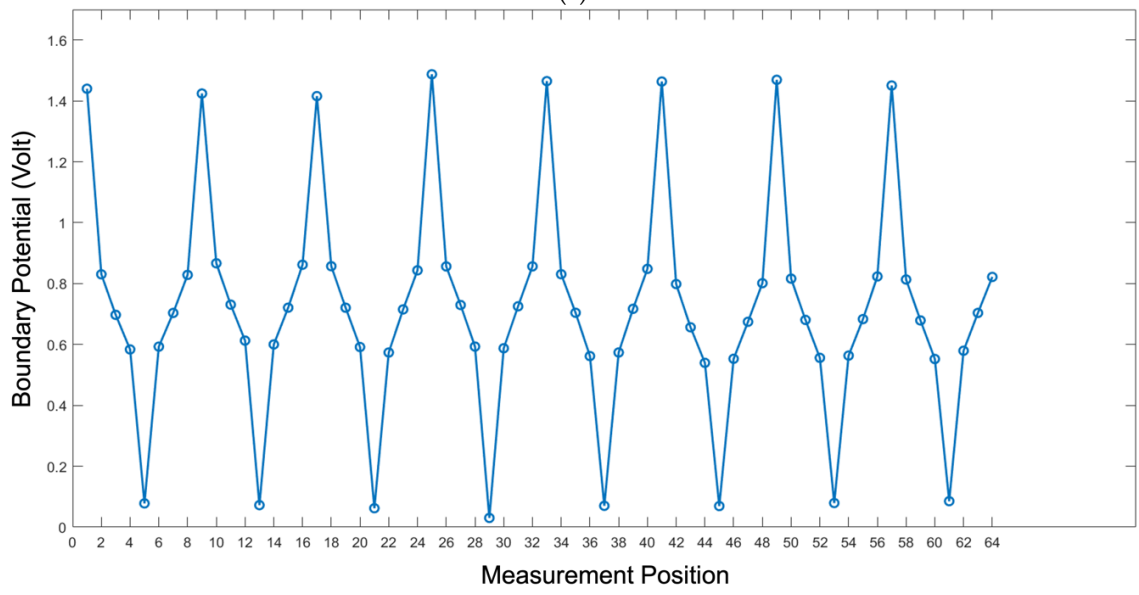

(b)

Figure 10. Boundary potential of mineral water using (a) adjacent method and (b) opposite method

Following acquiring reference data, an isolator is placed inside the container, specifically positioned in front of electrode 3. Then, the whole data acquisition process is run from the GUI. Figures 11(a) and 11(b) show the boundary potential value acquired compared to the reference data using the two current injection methods.

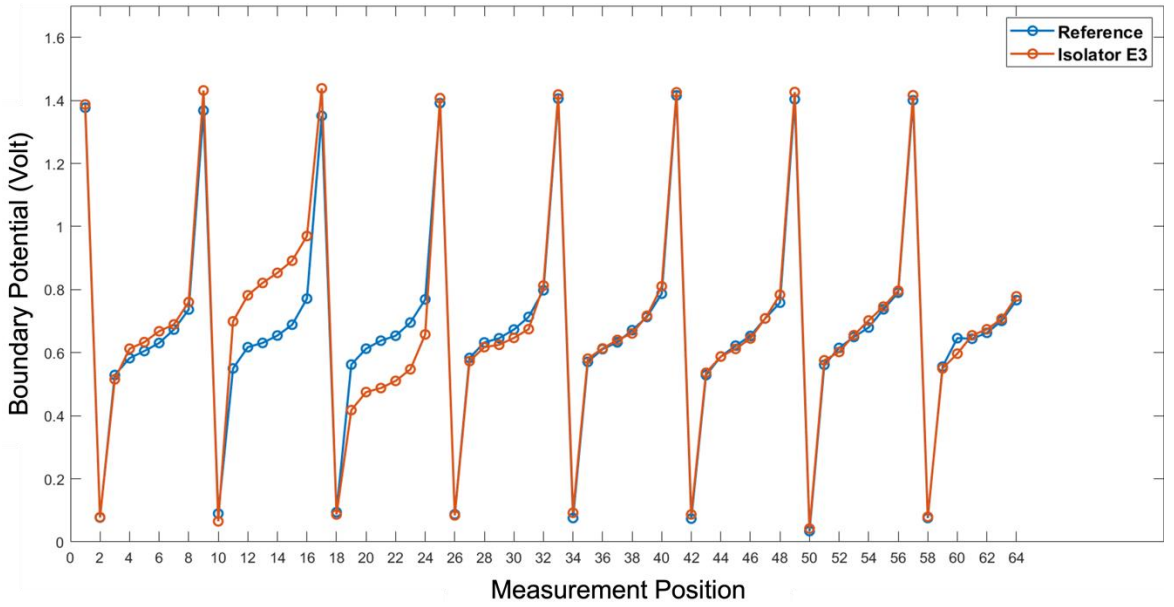

(a)

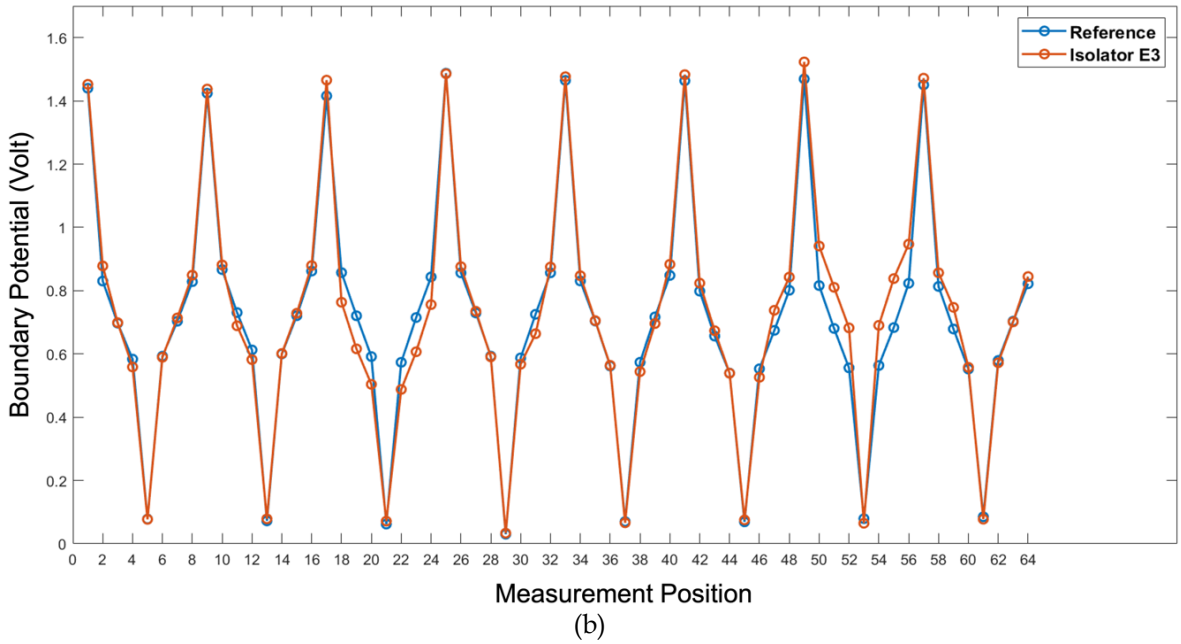

(b)

Figure 11. Boundary potential value with isolator using (a) adjacent and (b) opposite method

Based on the graph, an inhomogeneity pattern can be seen as a potential value drop and rise. In Figure 11(a), a potential rise occurred at the second electrode (one electrode before the object) by 0.1840 volts, and a potential drop occurred at the third electrode by 0.1391 volts. In Figure 11(b), a potential drop occurs at the third electrode by 0.0946 volts, and a potential rise occurs at the seventh electrode (opposite electrode from the object) by 0.1312 volts. When comparing the two current injection methods, each result shows a unique pattern representing inhomogeneity in the container. The voltage drop and rise are caused by the tendency of electrical currents to flow through a lower resistance path. When an inhomogeneous object is placed in the container, it causes a change in the resistivity distribution of the container, which causes the current to flow in a different direction and affects the potential value inside the container. In this case, current flows more through the solute and deflects from the isolator.

After the isolator data has been acquired, the isolator object is removed from the container, and a conductor object is placed in the container instead, specifically in front of electrode 7. Then, the whole data acquisition process is run from GUI. Figures 12(a) and 12(b) show the boundary potential value acquired compared to the reference data using the two current injection methods. Based on the graph, an inhomogeneity pattern can also be seen as a potential value drop and rise. In Figure 12(a), a potential drop occurs at the sixth electrode (one electrode before the object) by 0.2030 volts and a potential increase at the seventh electrode by 0.1444 volts. In Figure 12(b), a potential drop occurs at the third electrode by 0.1914 volts (opposite electrode from the object), and a potential rise occurs at the seventh electrode by 0.1606 volts.

When compared between the two current injection methods, each result shows a unique pattern representing inhomogeneity in the container. However, the result from the opposite injection method might be an issue. The pattern shown in Figure 12(b), which represents the inhomogeneity object at electrode 7, is coincidentally like the pattern shown in Figure 11(b), which represents the inhomogeneity object at electrode 3. This may be caused by the positioning of both objects, which are opposite. This issue is confusing when determining whether the inhomogeneity is an isolator or a conductor.

The final experiment to investigate the performance of the designed data acquisition system involved placing the isolator and conductor together. The isolator was placed near electrode 3, while the conductor was near electrode 7. The results are shown in Figure 13.

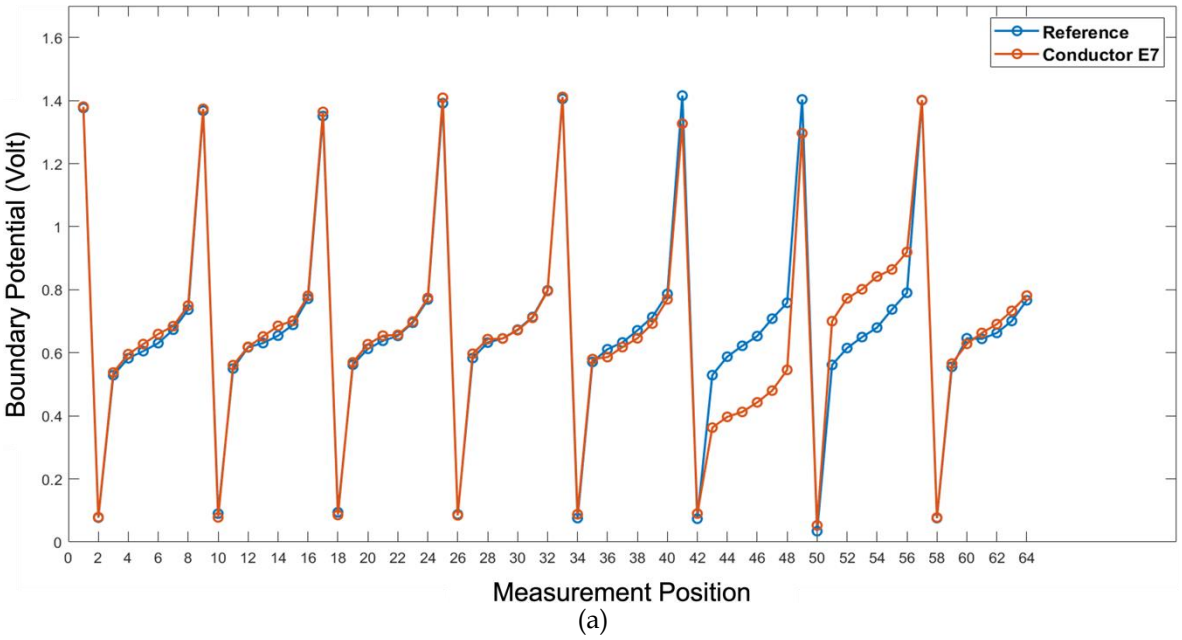

(a)

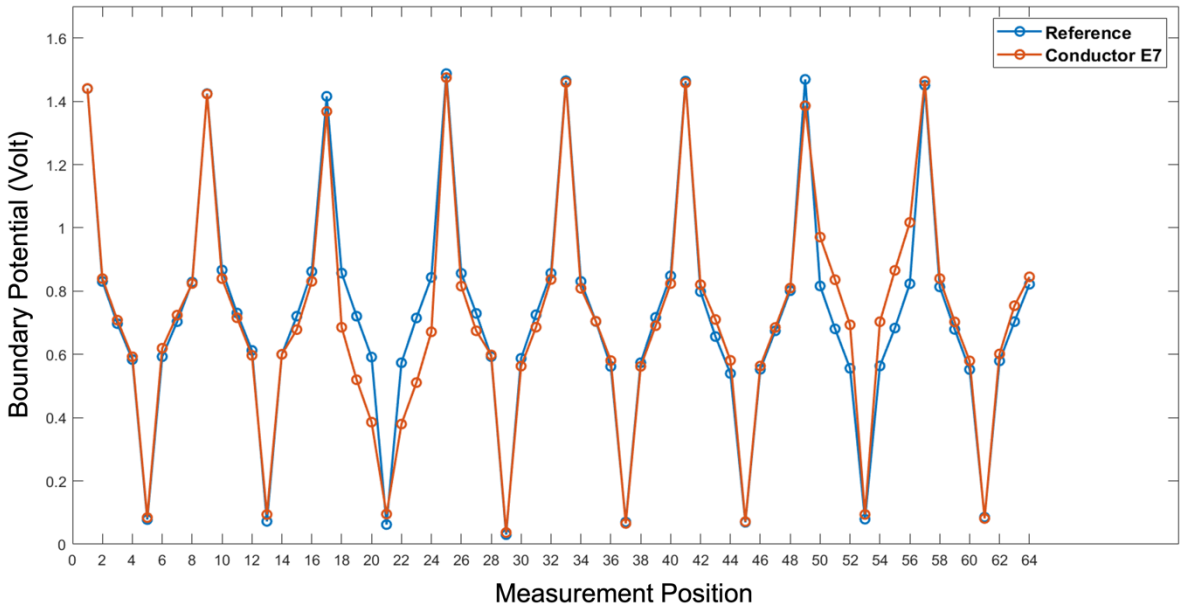

(b)

Figure 12. Boundary potential value with conductor using (a) adjacent and (b) opposite method

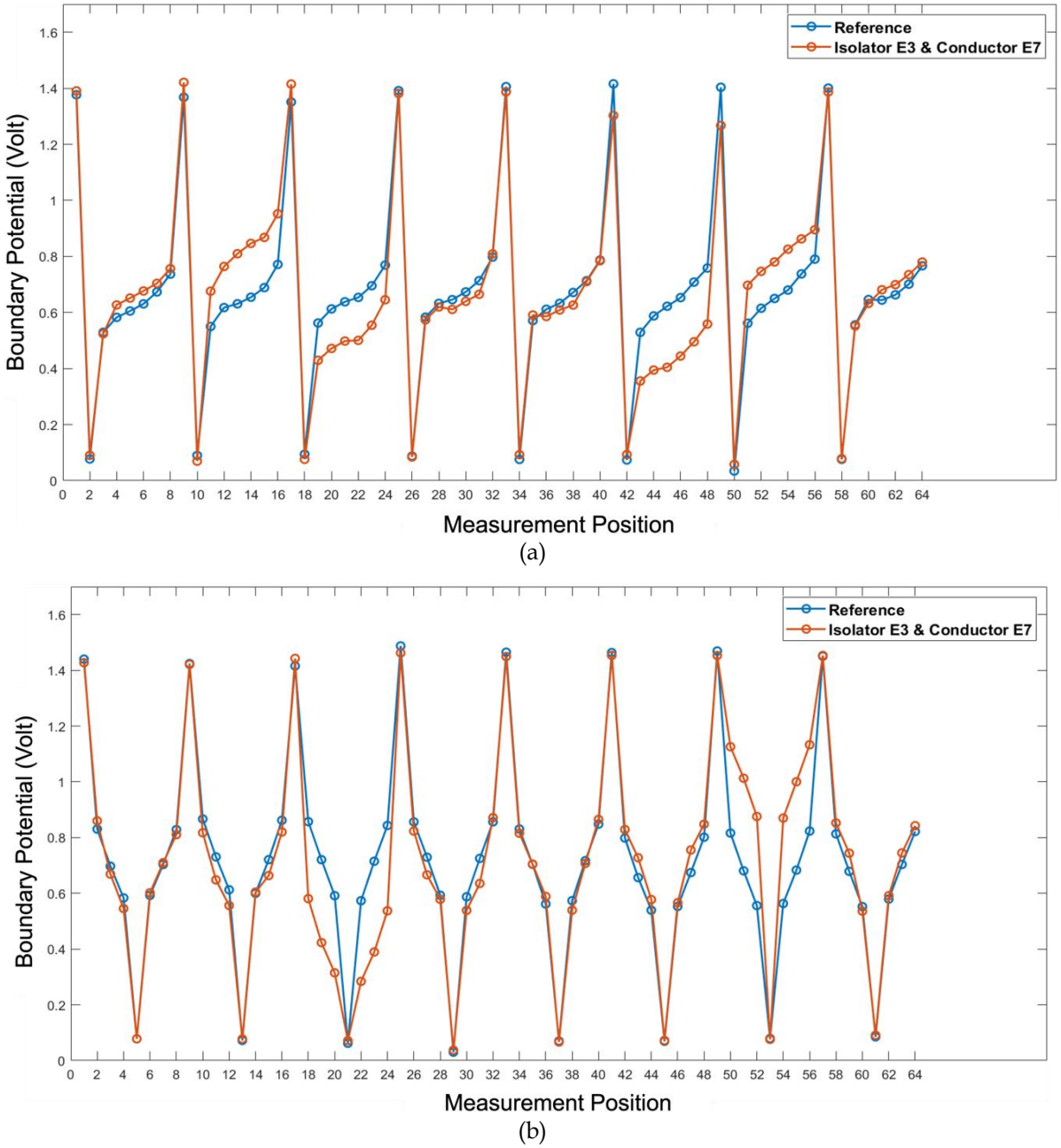

Figure 13. Boundary potential with isolator and conductor using (a) adjacent and (b) opposite method

According to the graph in Figure 13, the inhomogeneity pattern was a combination of the influence of objects such as isolators and conductors with values relative to the reference mineral water. In the adjacent current injection method (Figure 13(a)), the inhomogeneity pattern is seen during the current injection process at electrode 2 and electrode 3 (measurement positions 9-16 and 17-24) for the isolator and at electrode 6 and electrode 7 (measurement positions 41-48 and 49-56) for conductor objects. Each pattern has the same shape as when the objects are placed individually. When current is injected through electrode 2 and electrode 7, there is an increase in the boundary potential value with an average increase value of 0.1672 volts and 0.1290 volts, respectively. When the current injection is done through

electrode 3 and electrode 6, there is a decrease in the value of the limit potential with an average decrease value of 0.1387 volts and 0.2010 volts, respectively.

In the opposite injection method (Figure 13(b)), the inhomogeneity pattern becomes apparent only during the current injection at electrodes 3 and 7 (measurement positions 9-16 and 49-56). This similarity arises because the inhomogeneity patterns for the isolator and conductor appear alike, leading to a combined pattern that looks the same. However, when both objects are placed together, the measured boundary potential values during current injection at electrode 3 and electrode 7 combine the values when each object is placed individually. Therefore, the measured values are higher or lower than the potential values when the objects are placed separately. When current is injected through electrode 3, the limit potential value decreases by 0.2953 volts. Conversely, when current is injected through electrode 7, the limit potential value increases by 0.3158 volts. In the opposite injection method (Figure 13(b)), the inhomogeneity pattern is only noticeable during the current injection process at electrodes 3 and 7 (measurement positions 9-16 and 49-56). This occurs because the inhomogeneity patterns for the isolator and conductor appear similar, resulting in a combined pattern that looks the same. However, when both objects are placed together, the boundary potential values measured during current injection at electrodes 3 and 7 combine the values when each object is placed individually. As a result, the measured values are either higher or lower than the potential values observed when the objects are placed separately. Specifically, injecting current through electrode 3 reduces the boundary potential value by 0.2953 volts, while injecting current through electrode 7 causes an increase of 0.3158 volts. At this point, the adjacent method provides better results in revealing the inhomogeneity pattern, showing distinct patterns for the isolator and conductor. Additionally, the adjacent method allows for identifying different inhomogeneous objects at various positions within the container.

In this research, boundary potential analysis only represented the presence of inhomogeneous objects based on the increase and decrease of potential. This analysis could not specifically show the exact conductivity distribution value. Such values can only be obtained after the image reconstruction process through conductivity distribution images in units of Siemens per meter (S/m). This reconstruction process usually requires specialized software such as EIDORS or pyEIT.

Conclusion

The developed GUI-based data acquisition system worked as intended and supported the two current injection methods well.

The designed hardware, which includes a V-to-I converter circuit, multiplexer, electrodes, peak detector, and filter circuit, demonstrated satisfactory performance in testing. The V to I converter circuit exhibited an average peak difference between voltage and current of 4.86%, and the peak detector circuit showed an average error of 0.69%. The multiplexer circuit consistently switched quickly, and the filter circuit maintained stability in the frequency range of 2 kHz to 62.5 kHz. The data acquisition system in the form of a GUI has been functioning well, as indicated by its ability to display changes in potential distribution when objects such as conductors or insulators are placed, both with the adjacent method and the opposite method. A comparison between the two methods shows that the adjacent method is a better current injection method for showing inhomogeneous patterns on the boundary potential graph. However, it should be noted that this study only used eight electrodes and simple, inexpensive instrumentation. The data acquisition system has worked adequately,

although the non-uniformity is only visible in graphs relative to mineral water. Therefore, this GUI-based data acquisition system has the potential to be further developed for image reconstruction.

Acknowledgment

This research was made possible with support from the Electronics and Instrumentation Laboratory of the Faculty of Mathematics and Natural Sciences at Mulawarman University and the valuable assistance of the Elins 2019 Team.

References

[1] P. Suetens, *Fundamentals of Medical Imaging*, 3rd ed. Belgium: Cambridge University Press, 2017.

[2] A. Adler and D. S. Holder, *Electrical Impedance Tomography: Methods, History and Applications*, 2nd ed. Bristol: CRC Press, 2022.

[3] S. Mansouri, Y. Alharbi, F. Haddad, S. Chabcoub, A. Alshrouf, and A. A. Abd-Elghany, 'Electrical Impedance tomography – Recent applications and developments', *J Electr Bioimpedance*, vol. 12, no. 1, pp. 50–62, 2021, doi: 10.2478/joeb-2021-0007.

[4] M. Wang, *Industrial Tomography: Systems and Applications*, 2nd ed. Cambridge: Elsevier Science, 2022.

[5] B. Pitaloka, A. Zarkasi, and D. R Santoso, 'Development of low cost EIT equipment for educational purposes', in *Journal of Physics: Conference Series*, Institute of Physics Publishing, Feb. 2019. doi: 10.1088/1742-6596/1153/1/012041.

[6] E. Teschner, M. Imhoff, and S. Leonhardt, *Electrical Impedance Tomography: The realisation of regional ventilation monitoring*, 2nd ed. Lübeck: Dräger Medical GmbH, 2015.

[7] C.-C. Chang *et al.*, 'Electrical impedance tomography for non-invasive identification of fatty liver infiltrate in overweight individuals', *Sci Rep*, vol. 11, no. 1, p. 19859, Oct. 2021, doi: 10.1038/s41598-021-99132-z.

[8] C. L. Yang, 'Electrical Impedance Tomography: Algorithms and Applications', Thesis, University of Bath, 2014.

[9] B. Lobo, C. Hermosa, A. Abella, and F. Gordo, 'Electrical impedance tomography', *Ann Transl Med*, vol. 6, no. 2, p. 26, 2018, doi: 10.1201/b12939.

[10] Y. Shi, Z. Yang, F. Xie, S. Ren, and S. Xu, 'The Research Progress of Electrical Impedance Tomography for Lung Monitoring', *Front Bioeng Biotechnol*, vol. 9, no. October, pp. 1–16, Oct. 2021, doi: 10.3389/fbioe.2021.726652.

[11] Y. Wu, F. F. Hanzaee, D. Jiang, R. H. Bayford, and A. Demosthenous, 'Electrical Impedance Tomography for Biomedical Applications: Circuits and Systems Review', *IEEE Open Journal of Circuits and Systems*, vol. 2, pp. 380–397, 2021, doi: 10.1109/ojcas.2021.3075302.

[12] S. Gschoßmann, Y. Zhao, and M. Schagerl, 'Development of data acquisition devices for electrical impedance tomography of composite materials', in *ECCM 2016 - Proceeding of the 17th European Conference on Composite Materials*, 2016, pp. 1–9.

[13] S. Nonn, M. Schagerl, Y. Zhao, S. Gschossmann, and C. Kralovec, 'Application of electrical impedance tomography to an anisotropic carbon fiber-reinforced polymer composite laminate for damage localization', *Compos Sci Technol*, vol. 160, no. 2018, pp. 231–236, May 2018, doi: 10.1016/j.compscitech.2018.03.031.

[14] D. D. J. Corona-Lopez, S. Sommer, S. A. Rolfe, F. Podd, and B. D. Grieve, 'Electrical impedance tomography as a tool for phenotyping plant roots', *Plant Methods*, vol. 15, no. 1, p. 49, Dec. 2019, doi: 10.1186/s13007-019-0438-4.

[15] Y. Zhang, R. Xiao, and C. Harrison, 'Advancing hand gesture recognition with high resolution electrical impedance tomography', *UIST 2016 - Proceedings of the 29th Annual Symposium on User Interface Software and Technology*, pp. 843–850, 2016, doi: 10.1145/2984511.2984574.

[16] J. Zhu *et al.*, 'EIT-kit: An Electrical Impedance Tomography Toolkit for Health and Motion Sensing', *UIST 2021 - Proceedings of the 34th Annual ACM Symposium on User Interface Software and Technology*, pp. 400–413, 2021, doi: 10.1145/3472749.3474758.

[17] Z. Wang, S. Yue, H. Wang, and Y. Wang, 'Data preprocessing methods for electrical impedance tomography: A review', *Physiol Meas*, vol. 41, no. 9, 2020, doi: 10.1088/1361-6579/abb142.

[18] J. P. Leitzke and H. Zangl, 'Low-power electrical impedance tomography spectroscopy', *COMPEL - The International Journal for Computation and Mathematics in Electrical and Electronic Engineering*, vol. 38, no. 5, pp. 1480–1492, 2019, doi: 10.1108/COMPEL-12-2018-0530.

[19] A. Widodo and Endarko, 'Design of low-cost and high-speed portable two-dimensional electrical impedance tomography (EIT)', *International Journal of Engineering & Technology*, vol. 7, no. 4, pp. 6458–6463, 2018, doi: 10.14419/ijet.v7i4.23298.

[20] T. K. Bera, 'Applications of Electrical Impedance Tomography (EIT): A Short Review', *IOP Conf Ser Mater Sci Eng*, vol. 331, no. 1, p. 012004, Mar. 2018, doi: 10.1088/1757-899X/331/1/012004.

[21] S. Russo, S. Nefti-Meziani, N. Carbonaro, and A. Tognetti, 'Development of a High-Speed Current Injection and Voltage Measurement System for Electrical Impedance Tomography-Based Stretchable Sensors', *Technologies (Basel)*, vol. 5, no. 3, p. 48, 2017, doi: 10.3390/technologies5030048.

[22] N. V Ranade and D. C. Gharpure, 'Design and development of instrumentation for acquiring electrical impedance tomography data', in *2015 2nd International Symposium on Physics and Technology of Sensors (ISPTS)*, IEEE, Mar. 2015, pp. 97–101. doi: 10.1109/ISPTS.2015.7220091.

[23] A. Adler and A. Boyle, 'Electrical impedance tomography: Tissue properties to image measures', *IEEE Trans Biomed Eng*, vol. 64, no. 11, pp. 2494–2504, 2017, doi: 10.1109/TBME.2017.2728323.

[24] F. Pennati *et al.*, 'Electrical Impedance Tomography: From the Traditional Design to the Novel Frontier of Wearables', *Sensors*, vol. 23, no. 3, pp. 1–21, 2023, doi: 10.3390/s23031182.

[25] Z. Wang, S. Yue, X. Liu, A. McEwan, B. Sun, and H. Wang, 'Estimating Homogeneous Reference Frame for Absolute Electrical Impedance Tomography through Measurements and Scale Feature', *IEEE Trans Instrum Meas*, vol. 70, 2021, doi: 10.1109/TIM.2020.3036076.

[26] Z. Xu *et al.*, 'Development of a Portable Electrical Impedance Tomography System for Biomedical Applications', *IEEE Sens J*, vol. 18, no. 19, pp. 8117–8124, 2018, doi: 10.1109/JSEN.2018.2864539.

[27] S. Aldar, S. Chavan, D. Patil, and P. Chimurkar, 'Instrumentation of Data Acquisition for EIT', *Int J Comput Appl*, vol. 177, no. 33, pp. 12–16, 2020, doi: 10.5120/ijca2020919799.

[28] A. Ansory, P. Prajitno, and S. K. Wijaya, 'Design and development of electrical impedance tomography system with 32 electrodes and microcontroller', *AIP Conf Proc*, vol. 1933, no. February 2018, 2018, doi: 10.1063/1.5023993.

[29] T. K. Bera and J. Nagaraju, 'A MATLAB-Based Boundary Data Simulator for Studying the Resistivity Reconstruction Using Neighbouring Current Pattern', *J Med Eng*, vol. 2013, pp. 1–15, May 2013, doi: 10.1155/2013/193578.

[30] T. Zhang, G. Y. Jang, Y. E. Kim, T. I. Oh, H. Wi, and E. J. Woo, 'Influence of current injection scheme on electrical impedance tomography for monitoring of the respiratory function of obese subjects', *J Appl Phys*, vol. 128, no. 17, p. 174902, Nov. 2020, doi: 10.1063/5.0022704.

[31] Z. Kamus, A. Nofrianto, Y. W. Satwika, E. Ekawati, and D. Kurniadi, 'Optimization of Object Injection Current in the Development of Electrical Impedance Tomography for Bone Fracture Detection', *J Phys Conf Ser*, vol. 2309, no. 1, p. 012034, Jul. 2022, doi: 10.1088/1742-6596/2309/1/012034.

[32] G. Singh, S. Anand, B. Lall, A. Srivastava, and V. Singh, 'Low-cost multifrequency electrical impedance-based system (MFEIBS) for clinical imaging: design and performance evaluation', *J Med Eng Technol*, vol. 42, no. 4, pp. 274–289, May 2018, doi: 10.1080/03091902.2018.1478008.

[33] M. Khalighi and M. Mikaeili, 'A floating wide-band current source for electrical impedance tomography', *Review of Scientific Instruments*, vol. 89, no. 8, 2018, doi: 10.1063/1.5028435.

[34] G. Singh, S. Anand, B. Lall, A. Srivastava, V. Singh, and H. Singh, 'Practical phantom study of low cost portable EIT based cancer screening device', in *2016 IEEE Long Island Systems, Applications and Technology Conference (LISAT)*, IEEE, Apr. 2016, pp. 1–6. doi: 10.1109/LISAT.2016.7494151.

[35] T. Sun, S. Tsuda, K.-P. Zauner, and H. Morgan, 'On-chip electrical impedance tomography for imaging biological cells', *Biosens Bioelectron*, vol. 25, no. 5, pp. 1109–1115, 2010, doi: https://doi.org/10.1016/j.bios.2009.09.036.

[36] Y. Granot and B. Rubinsky, 'Frequency Marked Electrodes in Electrical Impedance Tomography', in *13th International Conference on Electrical Bioimpedance and the 8th*

Conference on Electrical Impedance Tomography, H. Scharfetter and R. Merwa, Eds., Berlin, Heidelberg: Springer Berlin Heidelberg, 2007, pp. 380–383.

[37] B. Gong, S. Krueger-Ziolek, and K. Moeller, 'An efficient classification-reconstruction method for 3D EIT imaging', *IFAC-PapersOnLine*, vol. 51, no. 27, pp. 36–40, Jan. 2018, doi: 10.1016/J.IFACOL.2018.11.604.

[38] L. Hongzheng, Y. Haiyan, S. Zhen, S. Shougang, and W. Kuan, 'Design of High Precision Digital AC Constant Current Source', 2018.

[39] L. Cao *et al.*, 'A novel time-difference electrical impedance tomography algorithm using multi-frequency information', *Biomed Eng Online*, vol. 18, no. 1, p. 84, 2019, doi: 10.1186/s12938-019-0703-9.

[40] R. Basak and K. A. Wahid, 'A Rapid, Low-Cost, and High-Precision Multifrequency Electrical Impedance Tomography Data Acquisition System for Plant Phenotyping', *Remote Sens (Basel)*, vol. 14, no. 13, Jul. 2022, doi: 10.3390/rs14133214.

[41] S. Mansouri, S. Chabchoub, Y. Alharbi, and A. Alshrouf, 'EIT 40-Electrodes Breast Cancer Detection and Screening', *IEEJ Transactions on Electrical and Electronic Engineering*, vol. 17, no. 8, pp. 1141–1147, Aug. 2022, doi: https://doi.org/10.1002/tee.23605.

[42] L. Yang *et al.*, 'Evaluation of adjacent and opposite current injection patterns for a wearable chest electrical impedance tomography system', *Physiol Meas*, vol. 45, no. 2, p. 025004, 2024, doi: 10.1088/1361-6579/ad2215.

[43] S. Egan and G. P. Curley, 'What is the role of PEEP and recruitment maneuvers in ARDS?', *Evidence-Based Practice of Critical Care*, pp. 50-56.e1, Jan. 2019, doi: 10.1016/B978-0-323-64068-8.00017-1.

[44] V. Tomicic and R. Cornejo, 'Lung monitoring with electrical impedance tomography: Technical considerations and clinical applications', Jul. 01, 2019, *AME Publishing Company*. doi: 10.21037/jtd.2019.06.27.

[45] L. Yang *et al.*, 'A Wireless, Low-Power, and Miniaturized EIT System for Remote and Long-Term Monitoring of Lung Ventilation in the Isolation Ward of ICU', *IEEE Trans Instrum Meas*, vol. 70, 2021, doi: 10.1109/TIM.2021.3085970.

[46] T. Zhang *et al.*, 'Advances of deep learning in electrical impedance tomography image reconstruction', Dec. 14, 2022, *Frontiers Media S.A.* doi: 10.3389/fbioe.2022.1019531.

[47] T. Zhang, G. Y. Jang, Y. E. Kim, T. I. Oh, H. Wi, and E. J. Woo, 'Influence of current injection scheme on electrical impedance tomography for monitoring of the respiratory function of obese subjects', *J Appl Phys*, vol. 128, no. 17, p. 174902, Nov. 2020, doi: 10.1063/5.0022704.

[48] T. K. Bera, A. Chowdhury, H. Mandai, K. Kar, A. Haider, and J. Nagaraju, 'Thin domain wide electrode (TDWE) phantoms for Electrical Impedance Tomography (EIT)', in *Proceedings of the 2015 Third International Conference on Computer, Communication, Control and Information Technology (C3IT)*, IEEE, Feb. 2015, pp. 1–5. doi: 10.1109/C3IT.2015.7060223.

[49] K. Liu *et al.*, 'Artificial Sensitive Skin for Robotics Based on Electrical Impedance Tomography', *Intelligent Systems*, pp. 1–13, Mar. 2020, doi: 10.1002/aisy.201900161.

[50] A. Widodo, A. Rubiyanto, and E. Endarko, 'The Influence of Multi-frequency Current Injection in Image Reconstruction for Two-Dimensional High-Speed Electrical Impedance Tomography (EIT)', *IPTEK The Journal of Engineering*, vol. 5, no. 1, pp. 5–8, 2019, doi: 10.12962/joe.v5i1.5019.